

## Article

# Additive Manufacturing of Bone Scaffolds Using PolyJet and Stereolithography Techniques

Shummaila Rasheed <sup>1,\*</sup>, Waqas Akbar Lughmani <sup>1</sup>, Muhannad Ahmed Obeidi <sup>2,3</sup>, Dermot Brabazon <sup>2,3</sup>   
and Inam Ul Ahad <sup>2,3</sup> 

- <sup>1</sup> Department of Mechanical Engineering, Capital University of Science and Technology, Islamabad 44000, Pakistan; dr.waqas@cust.edu.pk
- <sup>2</sup> I-Form, the SFI Research Centre for Advanced Manufacturing, Dublin City University, Dublin 09, Ireland; muhannad.ahmedobeidi@dcu.ie (M.A.O.); dermat.brabazon@dcu.ie (D.B.); InamUl.Ahad@dcu.ie (I.U.A.)
- <sup>3</sup> School of Mechanical and Manufacturing Engineering, Dublin City University, Dublin 09, Ireland
- \* Correspondence: shummaila@cust.edu.pk; Tel.: +92-340-802-7445

**Abstract:** In this study, the printing capability of two different additive manufacturing (3D printing) techniques, namely PolyJet and micro-stereolithography ( $\mu$ SLA), are investigated regarding the fabrication of bone scaffolds. The 3D-printed scaffold structures are used as supports in replacing and repairing fractured bone tissue. Printed bone scaffolds with complex structures produced using additive manufacturing technology can mimic the mechanical properties of natural human bone, providing lightweight structures with modifiable porosity levels. In this study, 3D scaffold structures are designed with different combinations of architectural parameters. The dimensional accuracy, permeability, and mechanical properties of complex 3D-printed scaffold structures are analyzed to compare the advantages and drawbacks associated with the two techniques. The fluid flow rates through the 3D-printed scaffold structures are measured and Darcy's law is applied to calculate the experimentally measured permeability. The Kozeny–Carman equation is applied for theoretical calculation of permeability. Compression tests were performed on the printed samples to observe the effects of the printing techniques on the mechanical properties of the 3D-printed scaffold structures. The effect of the printing direction on the mechanical properties of the 3D-printed scaffold structures is also analyzed. The scaffold structures printed with the  $\mu$ SLA printer demonstrate higher permeability and mechanical properties as compared to those printed using the PolyJet technique. It is demonstrated that both the  $\mu$ SLA and PolyJet printing techniques can be used to print 3D scaffold structures with controlled porosity levels, providing permeability in a similar range to human bone.



**Citation:** Rasheed, S.; Lughmani, W.A.; Obeidi, M.A.; Brabazon, D.; Ahad, I.U. Additive Manufacturing of Bone Scaffolds Using PolyJet and Stereolithography Techniques. *Appl. Sci.* **2021**, *11*, 7336. <https://doi.org/10.3390/app11167336>

Academic Editor: Marco Mandolini

Received: 16 July 2021

Accepted: 3 August 2021

Published: 9 August 2021

**Publisher's Note:** MDPI stays neutral with regard to jurisdictional claims in published maps and institutional affiliations.



**Copyright:** © 2021 by the authors. Licensee MDPI, Basel, Switzerland. This article is an open access article distributed under the terms and conditions of the Creative Commons Attribution (CC BY) license (<https://creativecommons.org/licenses/by/4.0/>).

**Keywords:** scaffold design; 3D-printed porous scaffold structures; trabecular bone; permeability; mechanical properties

## 1. Introduction

Although natural human bones have characteristics that allow them to regenerate and heal naturally, these characteristics are often not effective for large bone defects and injuries resulting from tumor resections, old age, and traffic accidents. These challenges in orthopedics pose significant risks to the health and quality of life of individuals [1,2]. Bone grafts such as autografts, allografts, and xenografts act as bone substitutes and are used in cases where a bone is unable to heal the defects caused by severe damage, trauma, deformity, or tumor [3]. Although natural bone grafts are biocompatible, osteoconductive, and osteoinductive, there are still limitations associated with their use, such as anatomical differences, lack of availability, risk of infection, and site morbidity [4–6]. To overcome the limitations associated with natural bone grafts, synthetic scaffolds have been developed. The materials used in the synthetic scaffolds are divided into four generations: first generation, composed of metals and alloys; second generation, composed of ceramics and polymers; third generation, composed of composites; fourth generation, composed of smart

materials [7]. In comparison with natural bone grafts, synthetic materials have drawbacks, including the manufacturability of complex structures [8], uncontrolled permeability [9], unmatched mechanical properties, high density (for metals), ion release from metals [10], the friability of ceramics [11], the low strength of polymers [12], and the uncontrollable degradation of composites [13]; however, smart nanoparticle-based composite materials can be used to control the degradation rate [7].

Synthetic bone scaffolds can be fabricated using a variety of methods, which are divided into two main categories, namely conventional and additive manufacturing techniques. The conventional techniques used for the fabrication of bone scaffolds are gas foaming, solvent casting, particle leeching, freeze drying, and electrospinning techniques. The conventional techniques also have shortcomings, including insufficient pore interconnectivity, inadequate pore size, and porosity and structure controllability [9]. Additive manufacturing technologies have led to noteworthy progress in the development of synthetic scaffolds for bone tissue engineering, as they provide defined pore interconnectivity, pore size, and porosity, as well as structural controllability. Additive manufacturing techniques used in bone tissue engineering include stereolithography (SLA), fused deposition modelling (FDM), selective laser sintering (SLS), and selective laser melting (SLM) [14,15]. According to ISO 52900, additive manufacturing fabrication is defined as a manufacturing process that employs an additive manufacturing technique, whereby successive layers or units are built up to form model. Synthetic bone scaffolds are not structurally equivalent to natural human bone because of the complex and heterogeneous physiological structures of native tissues. The literature is particularly focused on the fabrication of simplified synthetic scaffolds instead of reproducing the internal microarchitecture of natural human bone, which would make synthetic scaffolds functionally equivalent in terms of their mechanical properties and architectural parameters for regeneration and repair. In this manner, additively manufactured synthetic scaffolds have been fabricated with well-characterized transport and mechanical properties using unit elements with different architectural parameters, such as the porosity, pore size, and pore shape [16]. The porosity, pore size, and pore shape of a synthetic scaffold are critical design parameters that not only affect the permeability, which can result in cell death, but which also affect the mechanical properties, which can result in insufficient load-bearing capacity. The parameter that mainly affect the transport and mechanical properties of synthetic bone scaffold is porosity [17].

Permeability has prime importance in synthetic bone scaffolds, and must be considered when designing a scaffold because it can affect cell migration, cell metabolism, and mass transport of oxygen and nutrients; furthermore, it must be kept within the range found in human bones [15]. Gibson et al. showed that experimentally measured and numerically calculated permeability increased with increases in pore size and porosity [18]. Melchels et al. displayed the effects of synthetic scaffold permeability fabricated from salt leaching and stereolithography on nutrient transportation by comparing the results from cell culturing and cell seeding experiments, showing better cell interconnectivity and enhanced cell proliferation in the center of the scaffold's interior [19]. Kemppainen et al. used experimental and computational approaches to examine the effects of permeability on bone production for PCL (poly 3-caprolactone) scaffolds printed from a Solidscape 3D printer. The results showed that cartilaginous tissue was well proliferated in the less permeable environment, while for bone tissue regeneration and cell differentiation, higher permeability was more promising [20]. Furumoto et al. investigated the relationships among the processing conditions, tensile strength, porosity, and permeability of synthetic scaffolds fabricated through SLS and showed that the permeability increases with increases in porosity [21]. With the help of experimental and numerical analyses of cancellous bone, Syahrom et al. proposed that there is a direct relationship between permeability, porosity, and surface area, and also found that structures with similar porosity can have different levels of permeability because of their different surface areas [22]. Ochoa et al. utilized Darcy's law to find out the permeability of foam replica porous synthetic scaffolds, the

permeability values of which were measured using deionized water and were similar to the permeability of human trabecular bone [23]. With the use of a micro-CT-based FE method and the experimentally verified Kozeny–Carman formulation, Sandino et al. showed a correlation between permeability and the trabecular bone microstructure with the use of a constant head permeameter [24]. Malachanne et al. developed a simple test rig consisting of a constant head to provide a constant hydraulic pressure on the top surface of a test sample, in which they determined the experimental permeability and the determined permeability as  $1.1 \times 10^{-10} \text{ m}^2$  [25]. Different test fluids have been used for this type of analysis, such as water and gasses. Chor et al. used gas as a test fluid in permeability analysis in his study to avoid pore blockage and hydrolysis [26]. Grimm et al. determined the permeability values for a human bone using raw linseed oil as a test fluid, which ranged between  $0.40 \times 10^{-9} \text{ m}^2$  and  $11 \times 10^{-9} \text{ m}^2$  [27]. Various experimental studies have been carried out to measure the intrinsic permeability of natural bone using water as a test fluid in different directions, with values lying between  $10^{-10} \text{ m}^2$  and  $10^{-9} \text{ m}^2$  [27–29]. The permeability values measured by authors in previous studies for human natural bone varied between  $10^{-11} \text{ m}^2$  and  $10^{-8} \text{ m}^2$  [29].

Synthetic bone scaffolds must have mechanical properties, such as the compressive strength and elastic modulus, similar to those of natural human bone to avoid the effects of stress shielding and osteoporosis [30]. Compression tests can be performed to investigate the mechanical properties of synthetic scaffolds. Melchels et al. numerically investigated the mechanical properties of poly(D, L-lactide-co-ε-caprolactone)–poly(D, L-lactide)-resin-based synthetic scaffolds in terms of the architectural parameters, with the results showing that the mechanical properties of the synthetic scaffolds were within the same range as those of human bone [31]. In addition to the load bearing properties, previous studies have also shown that the cyclic mechanical loading of human bone can affect the blood content of bone, and in turn the shear strength [32]. It is evident from the above listed studies that the permeability and mechanical properties of synthetic bone scaffolds are two critical factors that must be evaluated and which should be within the same range as those of human bone to fulfil the mechanical and biological requirements of natural human bone.

Additive manufacturing techniques, such as fused deposition modeling (FDM), selective laser sintering (SLS), stereolithography (SLA), and material jetting (MJ), have different dimensional accuracy levels that can affect the final dimensions of the printed samples [33]. FDM, SLA, and SLS techniques have dimensional accuracy levels of 0.16%, 0.15%, and 0.11% and lower limits of  $\pm 0.2 \text{ mm}$ ,  $\pm 0.01 \text{ mm}$ , and  $\pm 0.3 \text{ mm}$ , respectively. MJ is the most accurate additive manufacturing technique, with dimensional accuracy of 0.5% and a lower limit of  $\pm 0.05 \text{ mm}$  [34].

In this paper, we assess the capability of two additive manufacturing techniques, Poly-Jet and microstereolithography ( $\mu\text{SLA}$ ), to 3D print synthetic scaffold structures with the desired porosity and mechanical properties. The permeability and mechanical properties of the printed scaffolds are investigated in detail. Numerical permeability calculations according to defined porosity and structural dimensions are validated via experimental results obtained from the 3D-printed scaffolds. The effects of the printing direction on the mechanical properties of the synthetic porous scaffolds were examined and the results are presented here.

## 2. Materials and Methods

### 2.1. Design and Development of 3D-Printed Scaffold Structures

Scaffolds are not structurally equivalent to natural human bone because of the complex and heterogeneous physiological structure of the native tissue; therefore, studies are needed focused on simple designs for scaffolds that are functionally equivalent to the tissue to be repaired in terms of the pore size, porosity, pore shape, and mechanical properties. Here, the pore sizes were chosen on the basis of cell responses. Three different porosity levels were chosen to reduce the mismatch between the stiffness of the scaffold and the native tissue in order to mitigate the stress shielding effect, while the pore shapes were chosen

that could offer the best mechanical properties. A healthy human bone contains pore size ranges from 300 to 600  $\mu\text{m}$  and even ranging up to 3000  $\mu\text{m}$  in cases of osteoporosis, with porosity ranges of 30–90% [35]. Keeping all of these points in mind, 3D CAD models of bone scaffold structures with cubic and hexagonal closed packed pore geometries were selected and designed with Creo Parametric 4.0 and SolidWorks. Cubic and hexagonal closed packed structures are the simplest porous unit cell designs, with all struts at angles of  $90^\circ$  and  $60^\circ$  to each other. Each CAD model was 15 mm in height and 30 mm in diameter, including the encased cylindrical structure (see Figures 1 and 2). The additively manufactured scaffolds had a maximum acceptable dimensional error of 0.54 mm, which is an acceptable dimensional error for the 3D printing of scaffolds [36]. Previous studies have shown that these cubic and hexagonal closed packed structures can meet the mechanical loading requirements of bone scaffolds [37–39]. Conventional manufacturing techniques, such as casting and injection molding, can be used to fabricate scaffolds with complex geometries; however, the use of computer-aided design (CAD) in additive manufacturing enables the fabrication of highly complex geometrical shapes for high-tech industries such as aerospace and biomedical engineering. In order to demonstrate the printing capabilities of the selected methods of additive manufacturing, 3D scaffold CAD models were designed for cubic and hexagonal closed packed structures, as presented in Table 1. Pore sizes were measured as the minimum diameter of the inscribed circle in hexagonal closed packed scaffold geometries and the inner length of the sides of the cube.

**Table 1.** Scaffold geometries designed for cubic and hexagonal closed packed structures (C, cubic structures; H, hexagonal closed packed structures; geometries marked with \* indicate the samples could not be printed due to smaller strut thickness).

Pore Size mm	Porosity Level					
	30%		50%		70%	
0.2	C *	H *	C *	H *	C *	H *
0.34	C	H *	C *	H *	C *	H *
0.6	C	H	C	H *	C *	H *
1.5	C	H	C	H	C	H
2.0	C	H	C	H	C	H
2.5	C	H	C	H	C	H
3.0	C	H	C	H	C	H

Figure 1a,c and b,d show the isometric and front views of the 3D CAD models of hexagonal closed packed and cubic pore geometry scaffold structures. Figure 1e,f represents the optical image of the 3D-printed scaffold structures taken using a Keyence Digital VHX-2000 microscope. Both cubic and hexagonal closed packed structures were encased into a cylindrical structure to clamp them into a rig designed for permeability testing.

Before 3DP, CAD models were saved in a simple, light, and easy-to-handle format, i.e., stl format, which is widely used in additive manufacturing. The PolyJet printer and stereolithography ( $\mu\text{SLA}$ ) printer were selected to print cubic and hexagonal closed packed scaffold structures. STRATASYS and ASIGA propose a large range of materials for 3D printing. In this study, commercially available VeroClear (STRATASYS) and PlasWhite (ASIGA) materials were chosen to print the scaffold structures.

For PolyJet 3D printing (3DP), the stl files of scaffold structures were sent to the PolyJet printer using integrated software. For the PolyJet printer, the time take to print the six scaffold samples was 90 min. All samples (28) were printed within 7 h. The printing time for the hexagonal pore geometry scaffold sample was slightly higher than the cubic pore geometry due to the complexity of the pore shape. After printing, the support material SUP706 was removed with a water jet at a pressure of 30 bars followed by compressed air cleaning at 4 bars for complete removal of residuals. It was observed that the PolyJet printer could not print several scaffold structures (marked as bold\* in the Table 1) due to the smaller strut thickness.

For stereolithography 3DP, the stl files of scaffold structures were sent to the  $\mu$ SLA printer using integrated software. It took three hours and twelve minutes for the  $\mu$ SLA printer to print a single scaffold at a time, with a slice thickness of 0.025 mm. The printed scaffold structures were first sonicated in isopropyl alcohol (IPA) for 20 min to remove the resinous material. Later, the solid support structures were removed by hand.

This study was more focused on investigating the effects of the different pore geometries on the compression performance of additively manufactured parts; hence, the input processing parameters were unified and kept constant so that a direct comparison could be carried out.

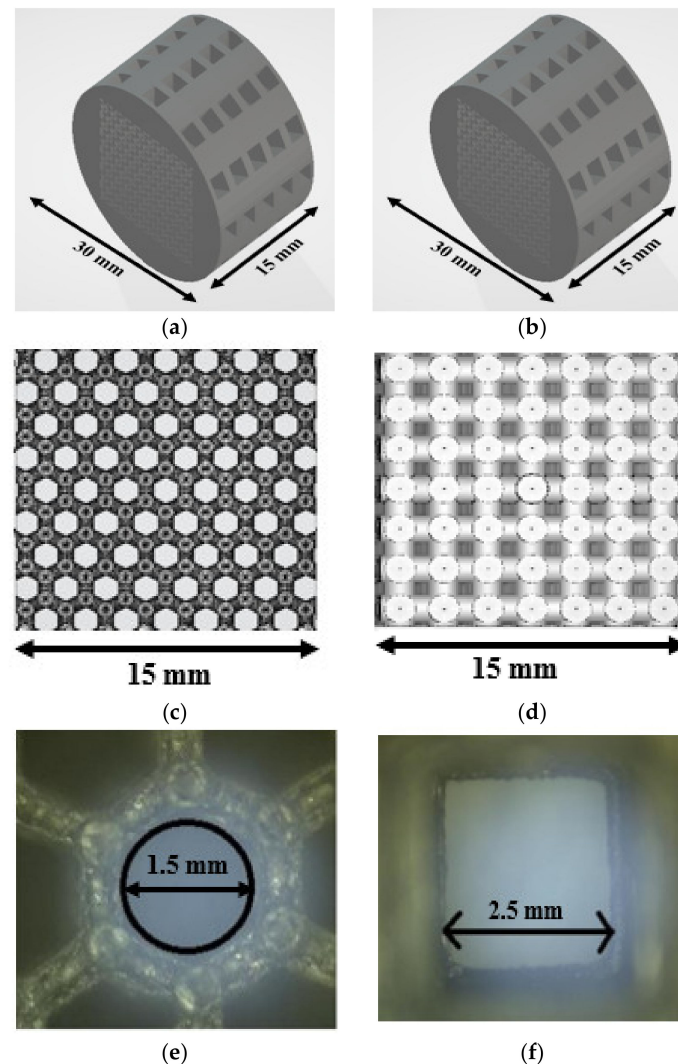


**Figure 1.** The 3D CAD models of the scaffold structures with hexagonal (H) and cubic (C) pore geometries: (a) isometric view and (c) front view of scaffold structure with hexagonal pore shape; (e) optical microscopic image of a 3D-printed scaffold with hexagonal pore shape; (b) isometric view and (d) front view of scaffold structure with cubic pore shape; (f) optical microscopic image of a 3D-printed scaffold pore of scaffold structure with cubic pore shape.

## 2.2. Permeability Analysis of 3D-Printed Scaffold Structures

### 2.2.1. Surface Energy Calculation

The surface energy and contact angle determine the hydrophobic properties of a material. Higher hydrophobicity for a scaffold material surface would result in increased permeability. The experimentally measured permeability could be affected by higher contact angles resulting from the surface energy of the material used in the development

of 3D scaffold structures. In order to analyze the effects of the contact angle and surface energy of the printed scaffolds on the fluid permeability through the pores, an FTA 200 dynamic contact angle analyzer was used to determine the contact angle using tap water, 15% glycerol water solution, and 20% glycerol water solution as test liquids.

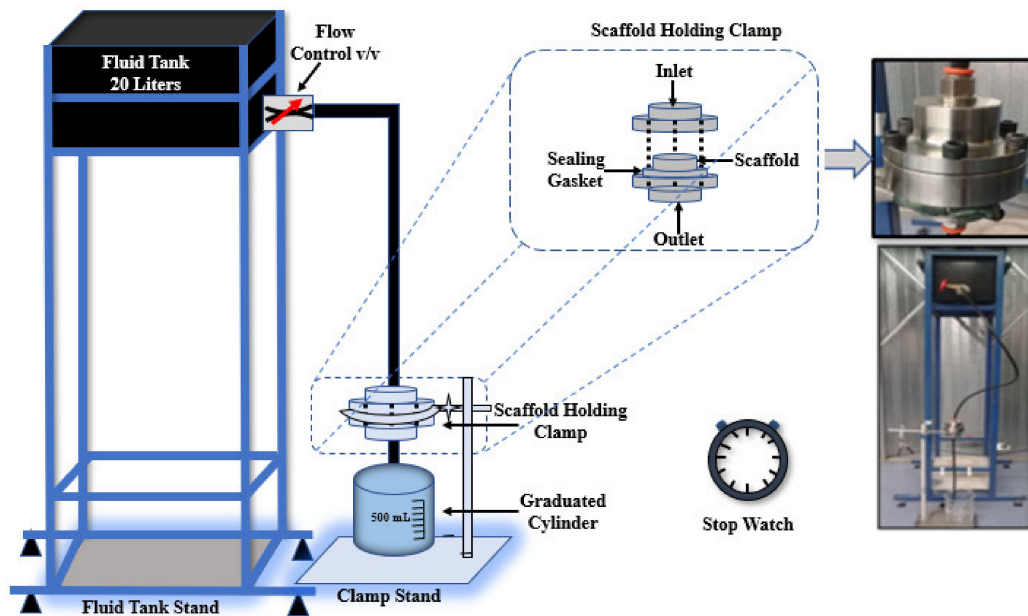


**Figure 2.** Experimental setup for the 3D-printed porous bone scaffold permeability analysis.

The sessile drop method was used to measure the contact angle. For this purpose, 5 mm high scaffold structures were modeled and printed using the PolyJet and  $\mu$ SLA printing techniques. The height of all scaffold structures shown in Figures 1 and 2 was 15 mm. The maximum working height of the FTA 200 dynamic contact angle analyzer was also 15 mm; therefore, for the complete formation of hanging drop and correct angle measurements, separate scaffold structures measuring 5 mm in height were printed, while keeping the rest of the dimensions the same. The scaffold structures were placed on a horizontal stage (in built direction) and 3  $\mu$ L of the probe liquid was dropped on the surface of the scaffold using a microsyringe with a flow rate of 1  $\mu$ L/s. Each reported value reflects an average of at least three measurements at three different positions on the 3D-printed sample surface. The measured contact angle was used for approximate surface energy values, along with the surface tension, polar, and dispersive components of each test liquids. Different models have been used for surface energy analysis, such as the Zisman critical wetting tension method, Girifalco method, Owens method, Wendt geometric mean method, Wu harmonic mean method, and Lewis acid–base theory [37]. Each model has certain limitations in terms of the angle limits and the number of test liquids used. In this study, the Zisman critical wetting tension model was used, which requires two test liquids and provides good estimations of the surface energy [37].

### 2.2.2. Numerical Calculations of Permeability

$$k = C * \frac{g}{\mu_w \rho_w} * \frac{e^3}{S^2 D_r^2 (1 + e)} \quad (1)$$

Here,  $k$  is the coefficient of permeability in  $m^2$ ;  $C$  is the constant, which takes into account the morphology of flow-through channels in a spongy media and has a value of 0.2 [38];  $e$  is the porosity;  $S$  is the specific surface area  $m^2/kg$ ;  $D_r$  = density of solid/density of fluid;  $\mu_w$  is the dynamic viscosity of water in Pa.s;  $g$  is the gravitational acceleration  $m^2/s$ ;  $\rho_w$  is the density of water in  $kg/m^3$ .

This equation can also be used to find out the intrinsic permeability  $K$  as follows:

$$k = K * \frac{\rho_w g}{\mu_w} \quad (2)$$

The Kozeny–Carman equation can be rearranged to express this in terms of permeability using (1) and (2):

$$K = \frac{C}{\rho^2} * \frac{e^3}{S^2 D_f^2 (1 + e)} \quad (3)$$

The density levels of PolyJet and  $\mu$ SLA materials are 1182–1920 kg/m<sup>3</sup> and 1182 kg/m<sup>3</sup>, respectively. From Equation (3), it can be seen that the fluid densities cancel each other out and the computed permeability results are independent of the fluid type.

### 2.2.3. Experimental Measurements of Permeability

To measure intrinsic permeability, a constant head permeability test setup was designed and developed, as shown in Figure 2. This setup consisted of a fluid holding tank with a 20 L capacity maintained at 800 mm above the surface of the scaffold to achieve hydrostatic pressure on the scaffold surface.

A clamping device was required that could hold the scaffold structures for the flow rate measurements. For this purpose, a stainless steel scaffold holding clamp and O-rings were designed according to the dimensions of the scaffold structures using Creo Parametric 4.0, which were machined using a high-precision CNC machine. To validate the clamp performance and tightness, a leak-tight test was performed on the clamp. For this test, a blind sample with similar dimensions to the scaffold dimensions was designed and three copies of the model were printed using the PolyJet printer. The leak-tight test was performed with tap water on the three blind samples under same conditions at which the permeability tests were carried out. The leak-tight test was performed for three hours and no leakages in the clamp were observed. The leak-tight test was performed after every few runs to check that the O-rings were still good and not flattened or damaged after several work cycles. The temperature of the laboratory was maintained at 22 °C as a requirement for other instruments in the lab. The ambience can affect the sample, test fluids, and sealants. Three different test fluids, including the tap water, 15% glycerol–water solution, and 20% glycerol–water solutions were selected to measure the permeability of the 3D-printed scaffold samples. These test fluids have also been used by others researchers for permeability analyses of different scaffold structures [23]. In previous studies, raw seed oil [39], olive oil [40], acrylic cement [41], silicone oil [14], and corn oil [42] were also used as test fluids. The purpose of using three different test fluid was to observe the effects of the viscosity of each fluid on the permeability. The two different water–glycerol solutions were prepared to simulate the viscosity of human blood without cells ranging from  $1 \times 10^{-3}$  Pa.s to  $1.3 \times 10^{-3}$  Pa.s [43]. For test fluids, glycerol was purchased from Alfa Aesar England. The viscosity of the prepared test fluids was measured with the help of the Physica MCR-301 Rheometer-Anton Paar instrument. Three samples of 3 mL were tested to measure the viscosity values for each test fluid. Every reading was taken for the 100th iteration and the obtained average viscosity levels of all fluids were about  $1 \times 10^{-3}$  Pa.s,  $2.35 \times 10^{-3}$  Pa.s, and  $2.87 \times 10^{-3}$  Pa.s for tap water, 15% glycerol–water, and 20% glycerol–water solutions, respectively, at 22 °C. The flow rate was measured by recording the time required for 500 mL to pass through the scaffold structures in only one direction (i.e., the sample-built direction). The cubic scaffold structures were omnidirectional and were, therefore, tested only in one direction. The hexagonal closed packed structures contained only one primary axis with less obstruction and were tested along this direction (built direction); thus, three readings of the times required for 500 mL of fluid to pass through each scaffold sample were recorded to obtain the average value, in order to ensure better flow rate results. The

same procedure was repeated for all the test fluids. Finally, to determine the experimental permeability using the measured results, Darcy's law was used:

$$k = \frac{q * l * \mu}{p * d} \quad (4)$$

where  $p$  is defined as:

$$p = \rho g \Delta h \quad (5)$$

where  $k$  is the permeability in  $m^2$ ,  $d$  is the total cross-sectional area in  $m^2$ ,  $q$  is volumetric flow rate  $m^3/s$ ,  $t$  is the time in s required to pass 500 mL through a sample,  $l$  is the length of the sample in m,  $h$  is the head of the fluid,  $\mu$  is the fluid dynamics viscosity Pa.s, and  $p$  is the pressure in Pa, calculated from Equation (5). The pressure and density values for the test fluids are provided in Table 2.

**Table 2.** Density and pressure values for the test fluids used in the permeability measurements.

Test Fluid	Tap Water	15% Glycerol–Water	20% Glycerol–Water
Density ( $kg/m^3$ )	998	1045	1060
Pressure (Pa)	7833	8192	8318

### 2.3. Design and 3D Printing of Standard Samples for Mechanical Testing

To evaluate the effects of the printing direction on the mechanical properties of the scaffold structures, two standard samples with circular and rectangular cross-sectional areas were designed using Creo Parametric 4.0 according to the ASTM D-695 (ISO 604) standard [44], as shown in Figure 3.



**Figure 3.** Standard samples with cylindrical and rectangular cross-sections.

The standard samples were 3D-printed and cleaned with the same procedure used for the PolyJet printer. Three copies of each standard sample were drawn in the  $x$ -,  $y$ -, and  $z$ -direction in the CAD file and printed in  $x$ -direction; hence, eighteen samples were printed in a single run. Figure 4 shows the printing direction of the standard samples, while the horizontal lines drawn on the sample surface representing the building layer direction with respect to the normal vector.

### 2.4. Mechanical Testing of Standard Blocks and 3D-Printed Scaffold Structures

Compression testing was performed following the ASTM D-695 (ISO 604) standard [44]. This is the standard test method used for compressive properties of rigid plastics. A Zwick/Roel Z50 universal testing machine integrated with the Zwick TestXpert simulation software was used to determine the compressive performance of the samples, with a maximum loading capacity of 50 kN.

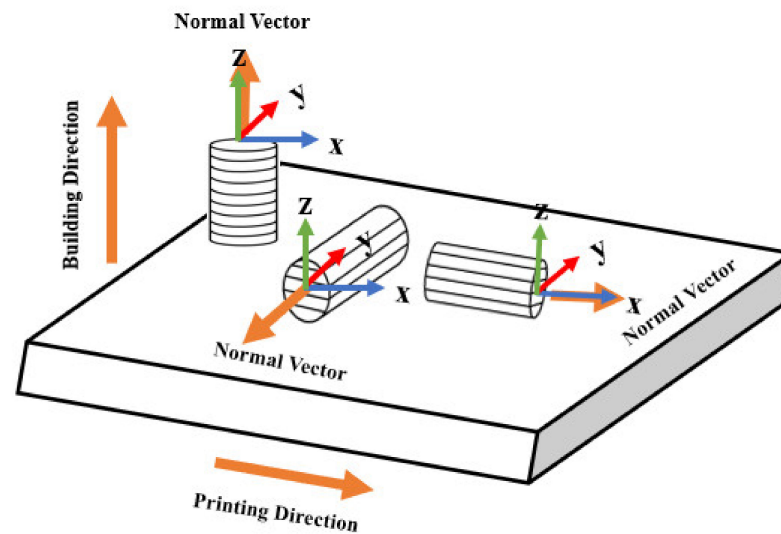


**Figure 4.** Standard samples drawn in  $x$ -,  $y$ -, and  $z$ -directions and printed in the  $x$ -direction, while lines on the sample shows the build layer.

Startrite-20RWF was used to cut the circular packing around the 3D-printed scaffold structures and a grinder was used to remove extra material to obtain the final samples for the compression test. After cutting and grinding the scaffold structures, the samples were subjected to a compression testing machine to determine the compressive strength, elastic moduli, and yield strength.

Force was applied with a compression speed of 2 mm/min and deformation in the samples was measured in the vertical direction. All specimens were compressed until failure. A standard force (N) versus displacement (mm) curve was plotted in the Zwick TestXpert simulation software. The force versus displacement curve data were extracted from the TestXpert software and later used in the formulae  $\sigma = \frac{F}{A}$  ( $\sigma$  = stress,  $F$  = force,  $A$  = area) and  $e = \frac{\delta}{L}$  ( $e$  = strain,  $\delta$  = length reduction,  $L$  = original length) to plot the stress–strain diagram for the scaffold structures. The stress strain diagram was used to determine the compressive properties of the scaffold structures.

The surface finish is of critical importance in bioimplant applications. The biocompatibility of the scaffolds and the long-term wear resistance and fatigue performance are crucial in such applications; however, since the current study was focused on the porosity and compression, the scaffolds were used directly after removing the support structure (as-built).

### 3. Results

#### 3.1. Contact Angle and Surface Energy Analyses

The surface energy analysis of PolyJet- and  $\mu$ SLA-printed scaffold structures showed that PolyJet 3D-printed scaffold structures had lower contact angles and higher surface energy values as compared to  $\mu$ SLA-printed scaffold structures. The higher contact angles resulted in lower surface energy values and increased the hydrophobic property of the 3D-printed scaffold structures. Increased hydrophobic properties result in increased permeability. Calculated values of contact angle and surface energy are presented in Table 3 given below.

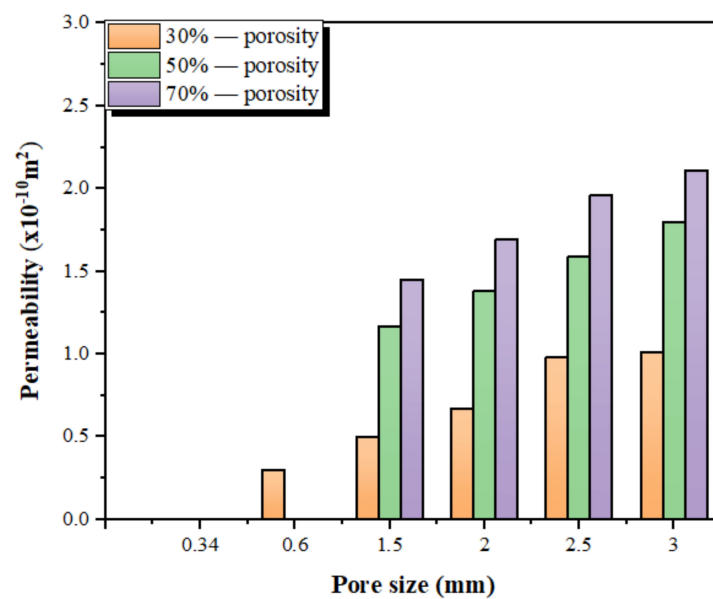
#### 3.2. Numerically Calculated Permeability

The numerically calculated permeability values showed that the cubic scaffold structures had higher permeability, ranging between 0.3 and  $2.4 \times 10^{-10} \text{ m}^2$ , as compared to the hexagonal closed packed scaffold structures, which ranged between 0.13 and  $2.0 \times 10^{-10} \text{ m}^2$ . The PolyJet 3D-printed scaffold structures and  $\mu$ SLA 3D-printed scaffold structures had the same calculated permeability because the Kozeny–Carman equation contains only structural properties. The specific surface area and porosity values are very critical factors, which varied with each scaffold

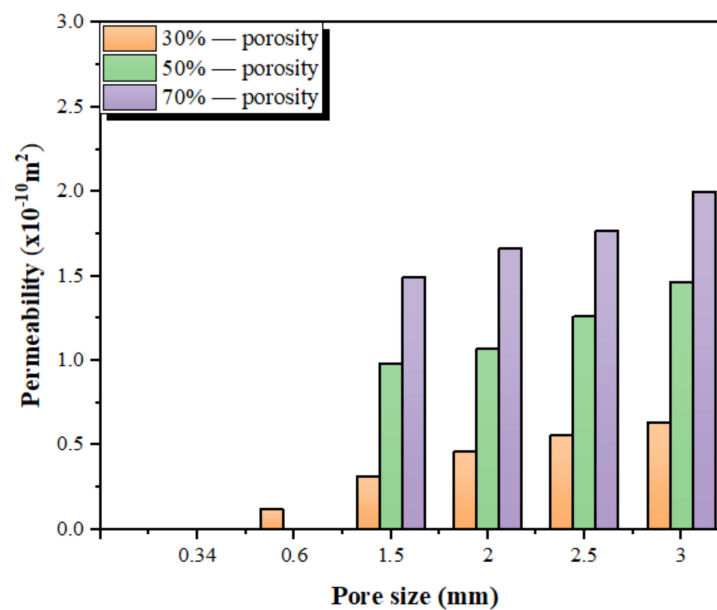
structure design and were obtained from CAD models. The CAD models were similar for both 3DP techniques used in this study. Figure 5 showed that the permeability was increased with the increases in pore size and porosity in both cubic and hexagonal closed packed scaffold structures.

**Table 3.** Contact angle and surface energy values for PolyJet (VeroClear) and  $\mu$ SLA (PlasWhite) 3D-printed scaffold structures.

Test Liquids	Contact Angle $^{\circ}$		Surface Energy mN/m	
	VeroClear	PlasWhite	VeroClear	PlasWhite
Tap Water	67.0	69.1	41.7	38.5
15% Glycerol–Water	70.0	72.6	40.0	37.9
20% Glycerol–Water	72.9	73.7	39.8	37.1



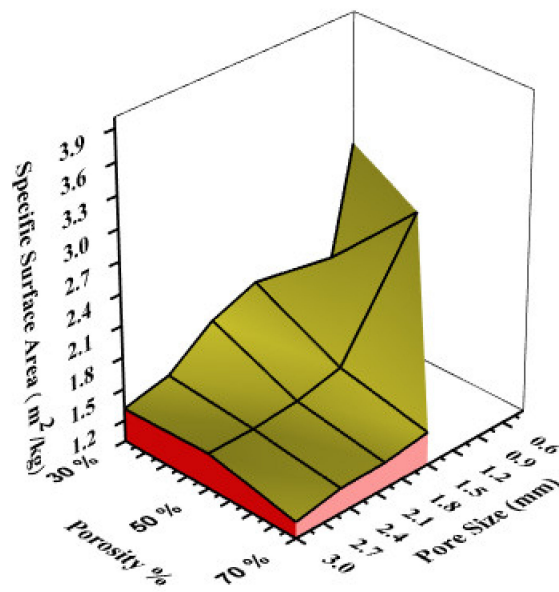
(a)



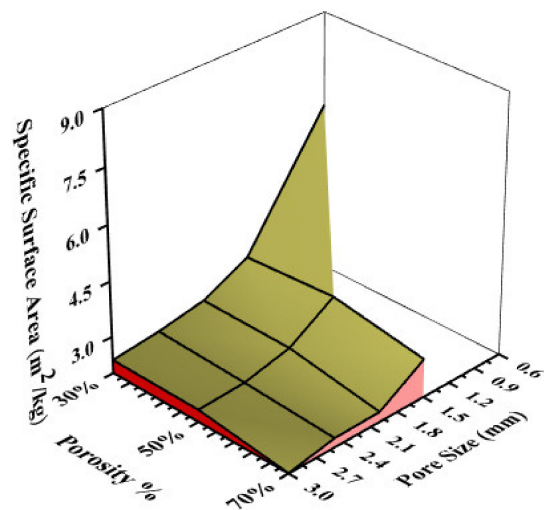
(b)

**Figure 5.** Numerically calculated permeability values: (a) Scaffold structures with cubic pore shape; (b) Scaffold structures with hexagonal pore shape.

Equation (3) showed that specific surface area was an important parameter that affected the permeability and changed with every scaffold structure; therefore, it was also important to observe the effects of the pore size and porosity of scaffold structures on the specific surface area, which ultimately affects the permeability. The surface area decreased with increases in pore size [45]. Figure 6 also shows the same results, i.e., the specific surface area decreases with increases in pore size and porosity. The lower pore sizes plotted in this figure were 0.34 mm and 0.6 mm and then 1.5 mm, 2.0 mm, 2.5 mm, and 3.0 mm; therefore, this drastic change in the surface area may also have been due to the difference in steps between 0.6 mm and 1.5 mm. Moreover, Equation (3) also represents the inverse relation between the porosity and surface area; hence, the increase in pore size decreased the specific surface area and resulted in increased permeability.



(a)

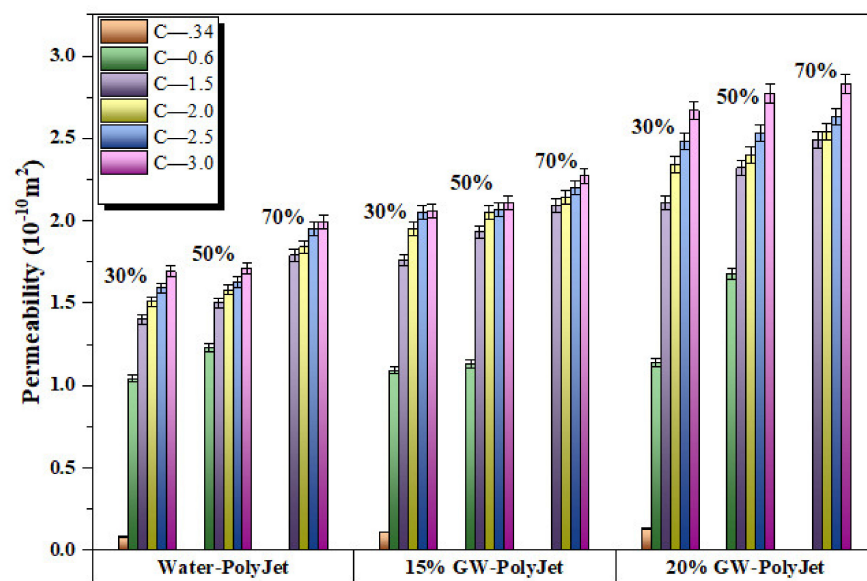


(b)

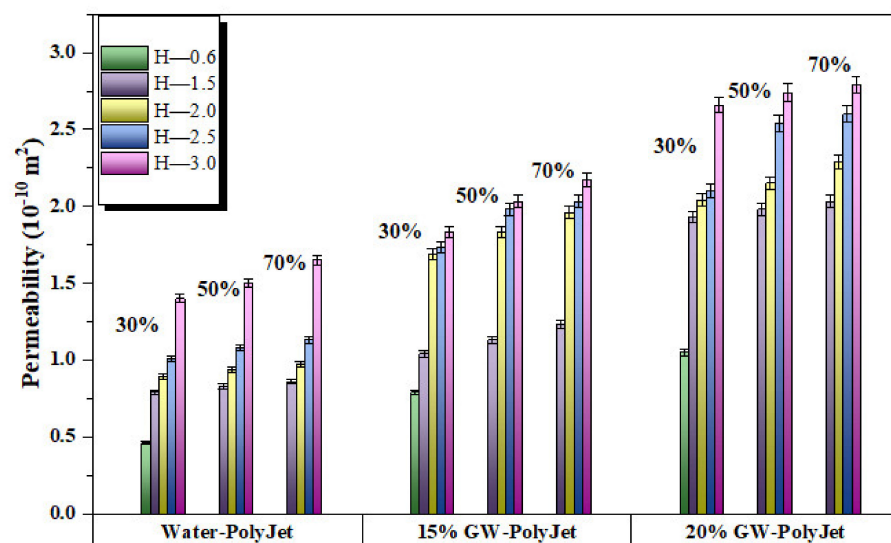
**Figure 6.** Specific surface area with respect to the pore size and porosity: (a) cubic structures; (b) hexagonal closed packed structures.

### 3.3. Experimentally Measured Permeability

Figure 7 presents the experimentally measured permeability of the PolyJet 3D-printed scaffold structures with cubic and hexagonal closed packed structures using tap water, 15% glycerol–water solution, and 20% glycerol–water solution. It can be observed from the figure that the experimentally measured permeability increased from lower to higher values in terms of the pore size, porosity, and viscosity of the test fluid. It was also noticed that the pore size had a greater effect on the permeability than the porosity and viscosity. The measured permeability values of cubic 3D-printed scaffold structures ranged between  $1.05$  and  $2.83 \times 10^{-10} \text{ m}^2$  (69% difference), while for hexagonal closed packed 3D-printed scaffold structures the values ranged between  $0.46$  and  $2.75 \times 10^{-10} \text{ m}^2$  (78% difference). Moreover, it was also observed that 3D-printed scaffold structures with the cubic pore shape had higher permeability values as compared to the 3D-printed scaffold structures with the hexagonal closed packed pore shape.



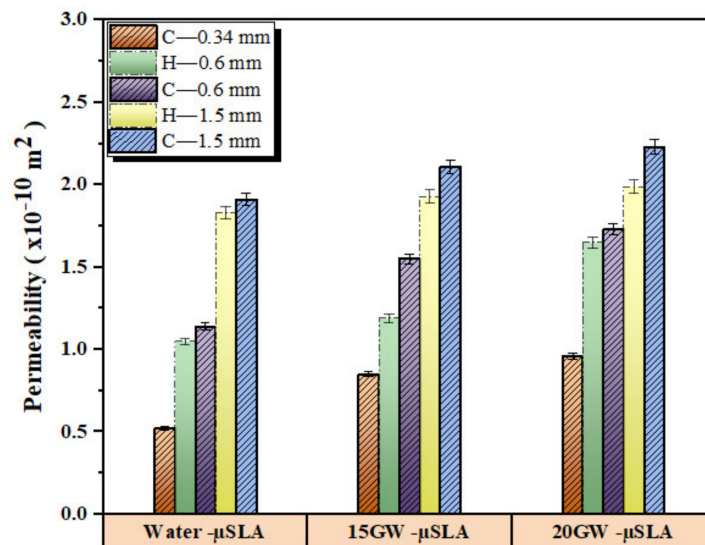
(a)



(b)

**Figure 7.** Experimentally measured permeability values for PolyJet 3D-printed scaffold structures using tap water, 15% glycerol–water solution, and 20% glycerol–water solution: (a) cubic structure; (b) hexagonal closed packed structure.

The  $\mu$ SLA-printed 3D scaffold structures showed similar results as for the PolyJet-printed samples in terms of permeability. Figure 8 shows the experimentally measured permeability values for the  $\mu$ SLA 3D-printed scaffold structures with cubic and hexagonal closed packed structures using tap water, 15% glycerol–water solution, and 20% glycerol–water solution. The measured permeability results demonstrated higher values for higher pore size, porosity, and viscosity values, and it was observed that the pore sizes had greater effects on permeability. The measured permeability values for cubic-pore-shaped  $\mu$ SLA 3D-printed scaffold structures ranged between  $0.52$  and  $2.23 \times 10^{-10} \text{ m}^2$  (76% difference) and for hexagonal closed packed 3D-printed scaffold structures ranged between  $1.05$  and  $1.99 \times 10^{-10} \text{ m}^2$  (47% difference) at 30% porosity.



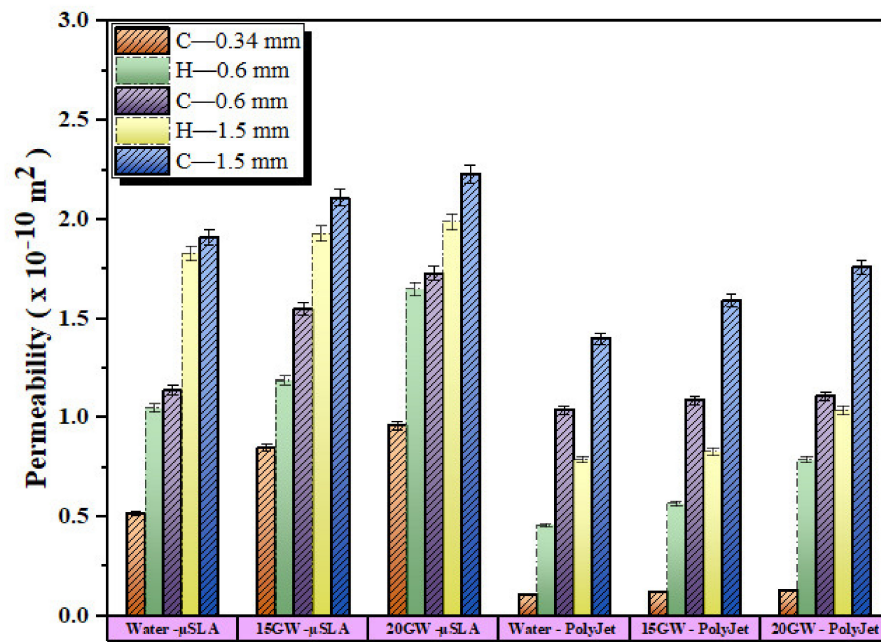
**Figure 8.** Experimentally measured permeability values for  $\mu$ SLA 3D-printed scaffold structures using tap water, 15% glycerol–water solution, and 20% glycerol–water solution at 30% porosity for both scaffold structures with cubic and hexagonal pore shapes.

Figure 9 shows a comparison between the experimentally measured permeability values for PolyJet and  $\mu$ SLA 3D-printed scaffold structures. As was mentioned in the development section, the  $\mu$ SLA-printed scaffold structures had greater precision because the  $\mu$ SLA-printed samples had higher permeability values as compared to the PolyJet-printed samples with lower pore sizes.

Table 4 shows that the experimentally measured permeability was higher than the numerically calculated permeability for all cases. The variation between the measured and calculated permeability values could be due to the poor cleaning of 3D-printed scaffold structures or due to the parameters that were not included in the Kozeny–Carman equation, such as pressure drop across the sample, fluid viscosity, and surface energy; therefore, a combined model with the benefits of both experimental and calculated methods could be beneficial for measuring permeability more accurately.

**Table 4.** Comparison between the measured and calculated values for cubic and hexagonal closed packed 3D-printed scaffold structures.

Permeability ( $\times 10^{-10} \text{ m}^2$ )	PolyJet		$\mu$ SLA	
	C	H	C	H
Measured	1.05–2.83	0.46–2.75	0.52–2.23	1.05–1.99
Theoretical	0.3–2.11	0.12–2.0	0.3–2.11	0.12–2.0



**Figure 9.** Experimentally measured permeability values for 3D-printed scaffold structures with cubic and hexagonal pore shapes using tap water, 15% glycerol–water solution, and 20% glycerol–water solution at 30% porosity.

### 3.4. Mechanical Properties of 3D-Printed Scaffold Structures

In this study, the mechanical properties of 3D-printed scaffold structures were investigated experimentally. In total, twenty-eight samples were used, and in order to determine the 95% confidence level, three repetitions of the compression test were performed for each sample; therefore, eighty-four samples (three copies of each sample) were printed to perform the compression tests. Figure 10 illustrates the stress–strain curves of the PolyJet 3D-printed scaffold structures in the uniaxial direction for different porosity levels and different pore sizes.

The results indicated that the 3D-printed scaffold structures deformed in a similar manner to ductile materials, except for the pore sizes of 2.0 mm, 2.5 mm, and 3.0 mm at 70% porosity. Similar trends were observed for the hexagonal closed packed PolyJet 3D scaffold structures, as shown in Figure 11.

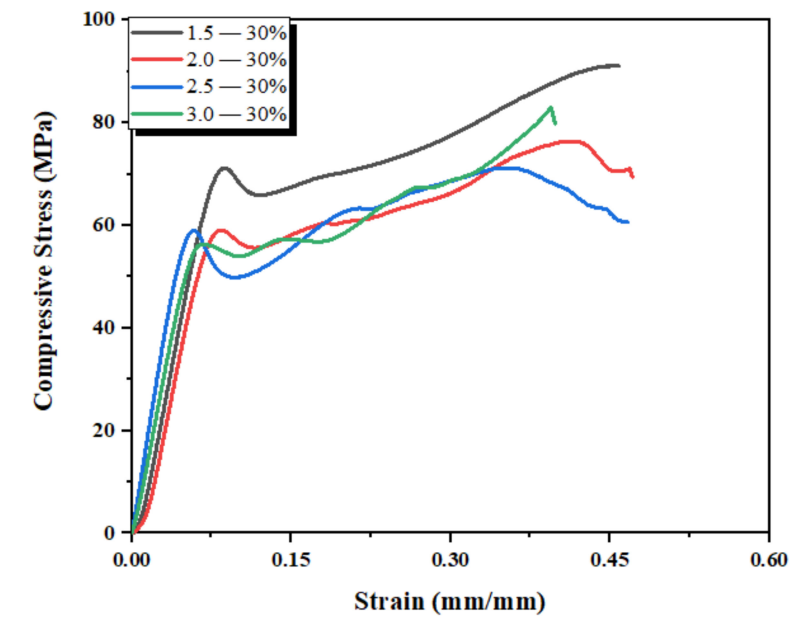
The elastic moduli and yield strengths of the PolyJet 3D-printed scaffold structures were calculated from the stress–strain curves and are presented in Table 5.

**Table 5.** Mechanical properties of PolyJet 3D-printed scaffold structures.

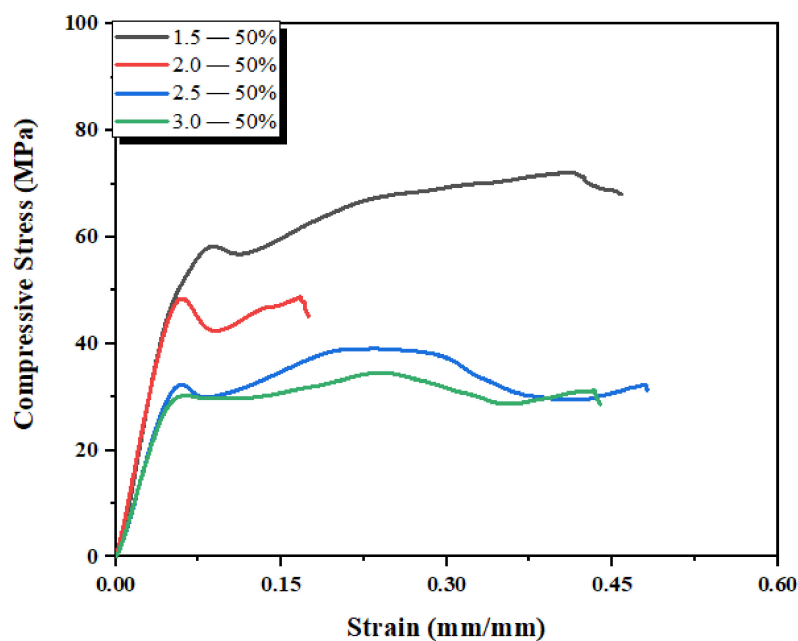
Pore Size (mm)	Elastic Modulus (GPa)						Yield Strength (MPa)					
	30%		50%		70%		30%		50%		70%	
	C	H	C	H	C	H	C	H	C	H	C	H
0.34	0.4	-	-	-	-	-	28	-	-	-	-	-
0.6	0.5	0.4	0.5	-	-	-	30	25	29	-	-	-
1.5	1.3	0.6	1.1	0.7	1.0	0.9	72	42	60	40	48	38
2.0	0.9	0.5	0.8	0.6	0.7	0.5	60	37	50	33	28	19
2.5	0.7	0.4	0.6	0.2	0.5	0.2	58	30	34	13	26	8
3.0	0.7	0.3	0.5	0.2	0.4	0.2	56	25	30	10	18	7.5

Table 5 shows that the elastic moduli and yield strength values for the PolyJet 3D-printed scaffold structures decreased with increases in porosity and pore size. Moreover, the cubic-pore-shaped 3D-printed scaffold structures offered higher elastic moduli and yield strength values as compared to the hexagonal closed packed 3D-printed scaffold structures.

The stress–strain curves for the  $\mu$ SLA-printed scaffold structures are presented in Figure 12, showing that the  $\mu$ SLA 3D-printed scaffold structures also deformed in a similar manner to ductile materials. The mechanical properties decreased with increases in porosity, similarly to the PolyJet 3D-printed scaffold structures.



(a)



(b)

Figure 10. Cont.

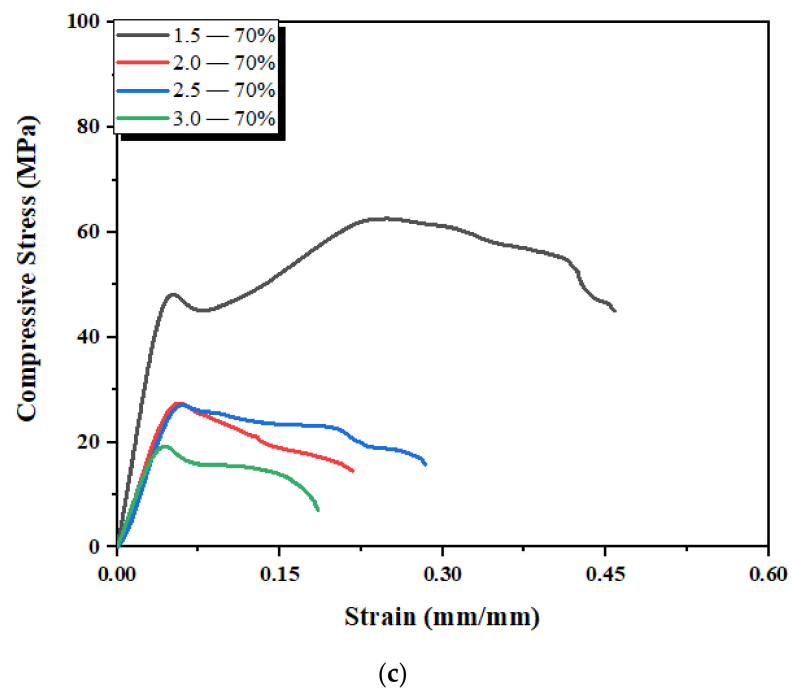


Figure 10. Stress–strain curves of PolyJet 3D-printed scaffold structures with a cubic pore shape at (a) 30%, (b) 50%, and (c) 70% with 1.5 mm, 2.0 mm, 2.5 mm, and 3.0 mm pore sizes.

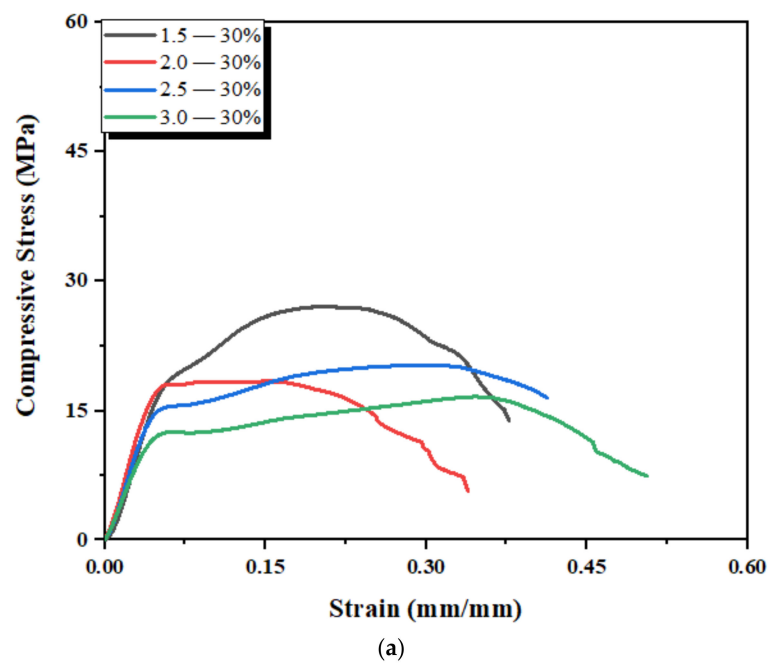
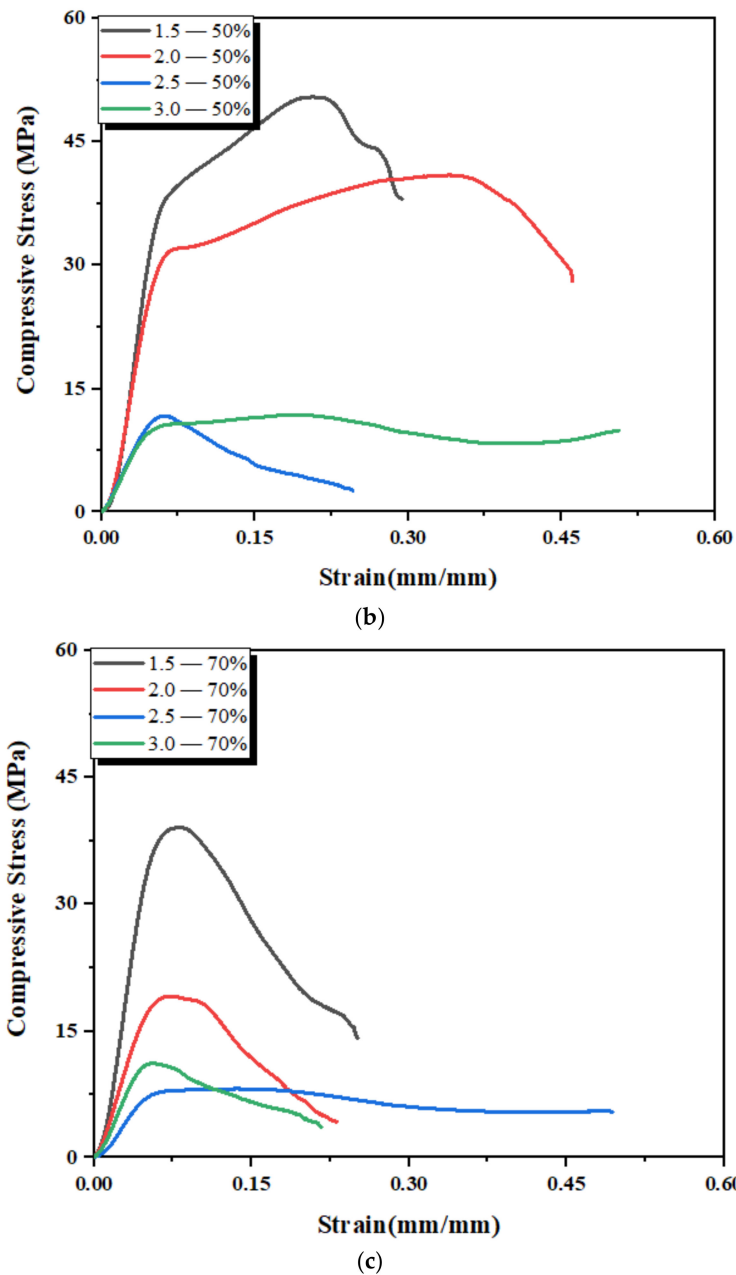
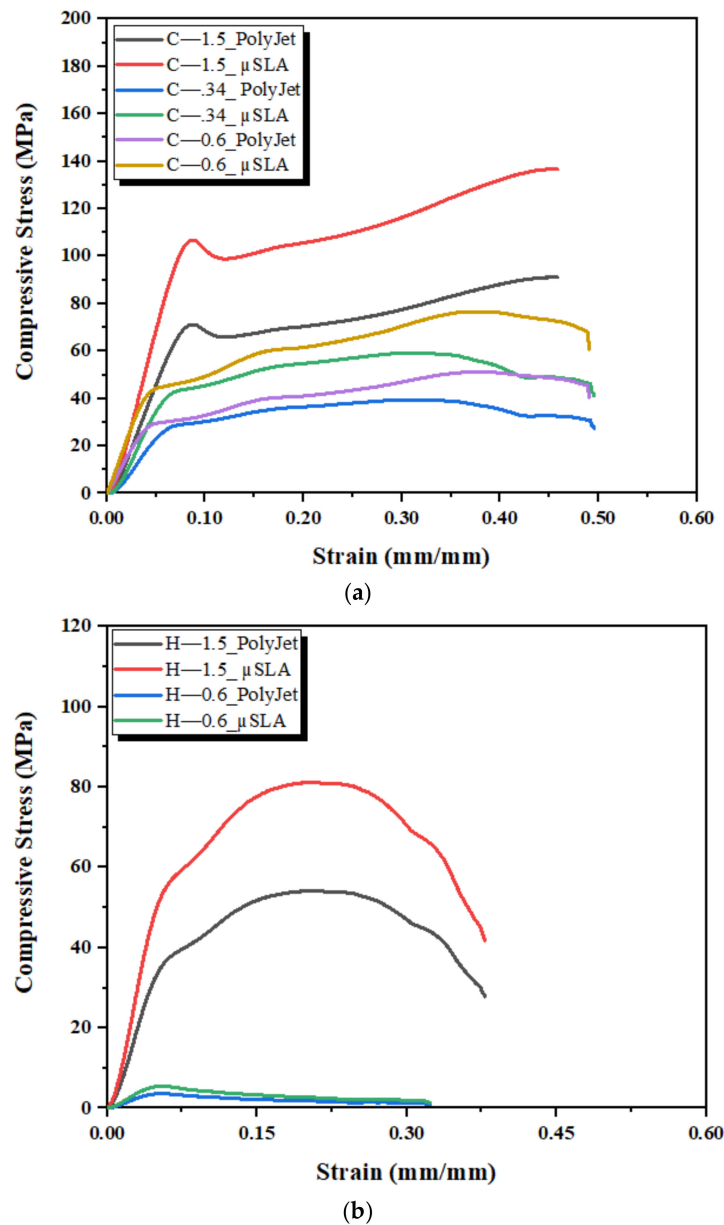


Figure 11. Cont.



**Figure 11.** Stress–strain curves of PolyJet 3D-printed scaffold structures with a hexagonal closed packed pore shape at (a) 30%, (b) 50%, and (c) 70% with 1.5 mm, 2.0 mm, 2.5 mm, and 3.0 mm pore sizes.

Figure 12 also shows a comparison between the PolyJet and  $\mu$ SLA 3D-printed scaffold structures. The mechanical properties of the  $\mu$ SLA-printed scaffold structures were 1.5 times higher than the PolyJet 3D-printed scaffold structures. Table 6 shows that the elastic moduli and yield strength of the  $\mu$ SLA 3D-printed scaffold structures also decreased with increases in the porosity and pore size. Moreover, the cubic-pore-shaped 3D-printed scaffold structures offered higher values for the elastic moduli and yield strength as compared to the hexagonal closed packed 3D-printed scaffold structures. The massive reduction in the mechanical properties of the scaffolds at pore size equal to 0.6 mm was due to the small strut thickness, which was 0.12 mm.



**Figure 12.** Stress–strain curves of the PolyJet and  $\mu$ SLA 3D-printed scaffold structures at 30% porosity: (a) cubic pore shape; (b) hexagonal closed packed pore shape.

**Table 6.** Mechanical properties of  $\mu$ SLA 3D-printed scaffold structures.

Mechanical Properties	Pore Shape	Pore Size (mm)		
		0.34	0.6	1.5
Elastic Modulus (MPa)	C	600	800	1900
	H	-	600	900
Yield strength (MPa)	C	42	45	108
	H	-	38	63

### 3.5. Mechanical Properties of 3D-Printed Standard Samples

The effects of the printing technique and printing direction on the mechanical properties of 3D-printed scaffold structures were studied with the help of standard samples. Figure 13 shows the stress–strain curves for PolyJet 3D-printed standard samples printed in

the  $x$ -,  $y$ -, and  $z$ -directions. The curves indicated that all of the PolyJet 3D-printed standard samples deformed in a similar manner to ductile materials. The mechanical properties were higher when the standard samples were printed in the  $z$ -direction.

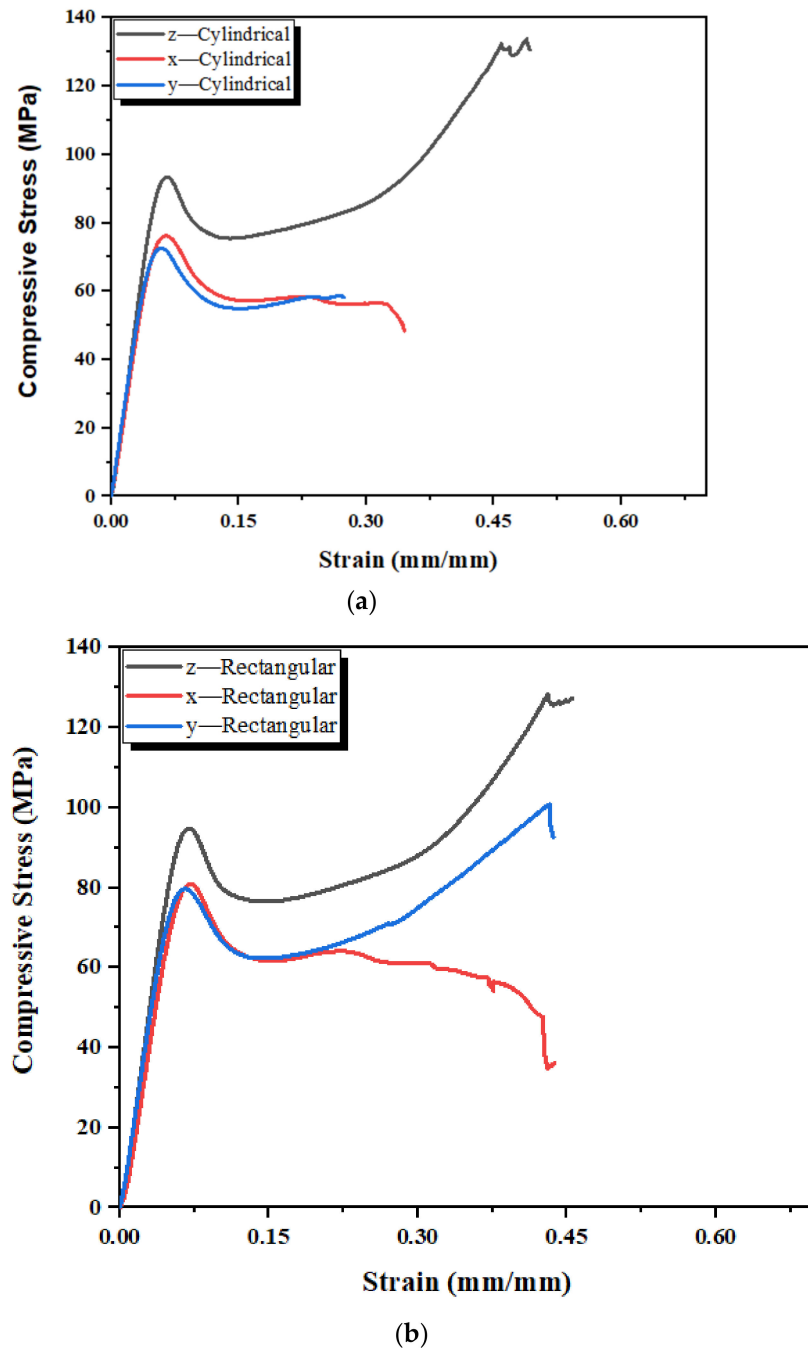


**Figure 13.** Stress–strain curves of 3D-printed standard samples in the  $x$ -,  $y$ -, and  $z$ -directions. (a) Standard sample with cylindrical cross-section; (b) Standard sample with rectangular cross-section.

Table 7 presents the elastic moduli and yield strength values of the standard samples printed in the  $x$ -,  $y$ -, and  $z$ -directions. The PolyJet samples printed in  $z$ -direction had higher mechanical properties than in the  $y$ - and  $x$ -directions.

**Table 7.** Mechanical properties of the 3D-printed standard samples.

Mechanical Properties (MPa)	Rectangular			Cylindrical		
	<i>x</i> -Direction	<i>y</i> -Direction	<i>z</i> -Direction	<i>x</i> -Direction	<i>y</i> -Direction	<i>z</i> -Direction
Elastic Modulus	1400	1300	1600	1300	1200	1600
Yield Strength	82	80	96	78	74	100

For the  $\mu$ SLA method, due to the build area limitation, the standard sample was printed only in the *z*-direction. The results of the compression test showed 1.3 times higher Young's modulus and yield strength values as compared to the PolyJet 3D-printed standard samples.

#### 4. Discussions

Various 3D-printed scaffold structures have been widely used in tissue engineering, especially in orthopedics for the replacement of damaged and diseased bone [39,40]. The mechanical properties of 3D-printed bone scaffold structures have to be such that they can withstand applied loads during daily activities. Apart from the mechanical properties, the transportation of nutrients, metabolic waste removal, and gaseous exchange through porous scaffolds are crucial. In 3D-printed scaffold structures, the porosity and pore size play pivotal roles, as these two parameters enable nutrient transportation through the structure for bone regeneration, in addition to providing adequate load-bearing capability to the structure. Therefore, the 3D printed scaffold structures must imitate the natural bone structure. The traditional manufacturing techniques do not provide design freedom to produce complex geometry structures. The use of additive manufacturing techniques such as PolyJet and  $\mu$ SLA enable the fabrication of porous scaffold structures with complex features and varied porosity. In this study, scaffold structures were printed using PolyJet and  $\mu$ SLA techniques. The application of these two techniques for 3D printing of trabecular bone scaffolds was evaluated based on the permeability and mechanical properties. Based on the results, it was observed that samples with a cubic pore shape produced via microstereolithography showed 0.7 times higher permeability compared to PolyJet-printed samples. For hexagonal closed packed samples, the microstereolithography results showed 1.5 times higher permeability comparing to PolyJet-printed samples; however, the  $\mu$ SLA technique has some limitations regarding the printing time and build area as compared to the PolyJet techniques. The experimentally measured and numerically calculated permeability values for 3D-printed scaffold structures manufactured using both techniques were found to be within the permeability range of bone in healthy individuals. The effects of the specific surface area and surface energy on the permeability of 3D-printed scaffold structures were analyzed. The obtained results demonstrated that an increased specific surface area results in decreased permeability; thus, the specific surface area of the scaffold plays a very important role, because porous structures with different geometries can have different specific surface areas with the same porosity. Several previous studies have been performed on the permeability levels of synthetic and natural bone porous structures, as summarized in Table 8.

**Table 8.** Comparison between intrinsic permeability values of natural human bone and synthetic porous scaffold structures.

Anatomic Region	Material Used	Fluid	Permeability $m^2$	Ref
Cancellous bone	Simulated cancellous bone	Simulated blood	$10^{-11}$ to $10^{-7}$	[22]
Human Vertebral body			$80.5 \times 10^{-10}$	
Human Proximal femur	Human cadaveric bone	Deionized water	$27.6 \times 10^{-10}$	[46]
Human Calcaneus			$35.4 \times 10^{-10}$	
Human, proximal tibia	Simulated cancellous bone	Simulated PMMA	$76.8 \times 10^{-10}$	[47]
Human calcaneal	Human cadaveric bone	Raw linseed oil	$4\text{--}109.7 \times 10^{-10}$	[27]
Human cadaveric lumbar			$4.899 \times 10^{-10}$	
Human vertebral body lumbar	Human cadaveric bone	Extra virgin olive oil	$10.7\text{--}109 \times 10^{-10}$	[48]
Human lumbar			$215\text{--}743 \times 10^{-10}$	
Corals	Coral samples	Water	$0.12\text{--}4.46 \times 10^{-9}$	[49]
$\mu$ SLA 3D-printed	Accura 60 resin	Water	$1.84\text{--}41.9 \times 10^{-10}$	[50]

The permeability levels and mechanical properties of 3D-printed scaffolds structures must match the mechanical properties of natural bone to avoid the stress shielding effect. The mechanical properties of the 3D-printed scaffolds manufactured using both techniques were in the range of healthy bone; however, the microstereolithography results indicated 1.3 times higher mechanical properties for these structures as compared to the PolyJet structures. For trabecular bone, the range of the elastic modulus is 0.2–2 GPa [51]. The yield strength is another important factor that must be taken into account for suitable 3D-printed scaffold structures. The Yield strength values for natural bone have been reported in numerous studies to be between 20 and 193 MPa [51].

In terms of the effects of the building direction on the mechanical properties of the 3D-printed scaffold structures, the possible parameters were extracted from the test data, i.e., the building direction, supports material, and UV exposure time. For the PolyJet technique, each layer is first cured using UV light and then the next layer is deposited, resulting in a laminated structure. The x- and y-directions are parallel to the applied load, while the layers built in the z-direction are perpendicular to the applied load; therefore, the building direction can have a significant effect on the mechanical properties of the synthetic scaffold structures. In this study, it was shown that the z-direction gives higher strength values than the x- and y-directions. When designing the 3D scaffold structures, the z-direction will provide higher mechanical strength in the final scaffold.

## 5. Conclusions

This research showed that microstereolithography is more precise than the PolyJet technique when printing complex shapes, although there was not a big difference between the permeability and mechanical strength values of the scaffold structures printed using both techniques; however, the microstereolithography method took more time to print a single scaffold structure with a limited scaffold size and geometry. On the other hand, with the PolyJet technique, multiple scaffold structures could be printed in a short time with a large range of sizes based on the build area. This study also showed that the pore size, porosity, and surface energy need to be controlled to acquire good permeability and mechanical strength values. The PolyJet-printed scaffold samples showed higher surface energy and higher contact angle values for higher-viscosity fluids as compared to the microstereolithography-produced scaffolds. Lower surface energy resulted in higher hydrophobicity and increased permeability. Furthermore, the results showed that the viscosity is also an important parameter for permeability calculations. Higher viscosity resulted in higher permeability values. The 20% glycerol–water solution had higher permeability values than the 15% glycerol–water solution or water alone. This could be

due to the higher flow path disorder of the lower viscosity fluid flow through the scaffold structures and the larger contact angles related to the hydrophobicity for the more viscous fluid. Equations (1) and (5) were used to determine the experimental and numerical permeability, respectively. The difference between the experimentally measured and numerically calculated permeability could be due the factors not considered in Equation (5), i.e., the effects of the viscosity and pressure. Equation (5) only included the structural factors, such as the porosity and specific surface area; with the help of this study, a combination of these two relations is suggested to determine the permeability values and to allow a good comparison between the measured and calculated permeability values. The effects of the scaffold architectural parameters on the permeability and load-bearing capacity values of the synthetic porous scaffolds investigated in this study will provide better information to allow the best-suited combination and best-suited 3D printing technique to be selected according to the requirements of the host body region in tissue engineering applications.

Additive manufacturing is opening new doors and allowing higher feature complexity to be achieved, which is required to provide the best solutions in tissue engineering. This study contributes towards tissue engineering applications regarding the selection of the architectural parameters needed to meet the required permeability and mechanical strength ranges using additive manufacturing. Although there are certain limitations in additive manufacturing, such as the material choice, this technique can be used to achieve complex features that are impossible to manufacture via conventional manufacturing processes.

The future steps in this field will be to perform studies on the modeling of scaffolds and to perform accelerated aging simulations to evaluate scaffold performance. In order to perform in vitro biocompatibility tests using human and model animal cells, coatings could be applied to the scaffolds. Regarding the proliferation and cytotoxicity, in vitro and in vivo biocompatibility tests can be performed. The sustainability of the scaffolds also needs to be investigated.

**Author Contributions:** Conceptualization, S.R., W.A.L., M.A.O., D.B. and I.U.A.; formal analysis, S.R., W.A.L., M.A.O., D.B. and I.U.A.; funding acquisition, I.U.A. and D.B.; investigation, S.R. and I.U.A.; methodology, S.R., W.A.L., M.A.O., D.B. and I.U.A.; project administration, I.U.A.; supervision, W.A.L., D.B. and I.U.A.; writing—original draft, S.R.; writing—review and editing, W.A.L., D.B. and I.U.A. All authors have read and agreed to the published version of the manuscript.

**Funding:** The authors acknowledge the financial support from the Key Action 1 Erasmus+ International Credit Mobility programme KA107-000598 2018–2020. This research is supported in part by a research grant from the Science Foundation Ireland (SFI) under grant number 16/RC/3872 and is co-funded under the European Regional Development Fund and by I-Form Industry partners. The authors acknowledge the financial support from the Faculty of Engineering and Computing, Dublin City University.

**Institutional Review Board Statement:** Not applicable.

**Informed Consent Statement:** Not applicable.

**Data Availability Statement:** All data is provided in the manuscript.

**Conflicts of Interest:** The authors declare no conflict of interest.

## References

1. El-Rashidy, A.A.; Roether, J.A.; Harhaus, L.; Kneser, U.; Boccaccini, A.R. Regenerating bone with bioactive glass scaffolds: A review of in vivo studies in bone defect models. *Acta Biomater.* **2017**, *62*, 1–28. [[CrossRef](#)]
2. Du, X.; Fu, S.; Zhu, Y. 3D printing of ceramic-based scaffolds for bone tissue engineering: An overview. *J. Mater. Chem. B* **2018**, *6*, 4397–4412. [[CrossRef](#)] [[PubMed](#)]
3. Campana, V.; Milano, G.; Pagano, E.; Barba, B.; Salonna, G.; Lattanzi, W.; Logroscino, G. Bone substitutes in orthopaedic surgery: From basic science to clinical practice. *J. Mater. Sci. Mater. Med.* **2014**, *25*, 2445–2461. [[CrossRef](#)] [[PubMed](#)]
4. Syahrom, A.; Abdul Kadir, M.R.; Abdullah, J.; Öchsner, A. Permeability studies of artificial and natural cancellous bone structures. *Med. Eng. Phys.* **2013**, *35*, 792–799. [[CrossRef](#)] [[PubMed](#)]

5. Zhao, F.; Vaughan, T.J.; Mcnamara, L.M. Multiscale fluid–structure interaction modelling to determine the mechanical stimulation of bone cells in a tissue engineered scaffold. *Biomech. Model. Mechanobiol.* **2015**, *14*, 231–243. [[CrossRef](#)]
6. Murugan, R.; Ramakrishna, S. Development of nanocomposites for bone grafting. *Compos. Sci. Technol.* **2005**, *65*, 2385–2406. [[CrossRef](#)]
7. Yunus Basha, R.; Sampath, S.K.; Doble, M. Design of biocomposite materials for bone tissue regeneration. *Mater. Sci. Eng. C* **2015**, *57*, 452–463. [[CrossRef](#)] [[PubMed](#)]
8. Bajaj, P.; Schweller, R.M.; Khademhosseini, A.; West, J.L.; Bashir, R. 3D biofabrication strategies for tissue engineering and regenerative medicine. *Annu. Rev. Biomed. Eng.* **2014**, *16*, 247–276. [[CrossRef](#)] [[PubMed](#)]
9. Chocholata, P.; Kulda, B.; Babuska, V. Fabrication of scaffolds for bone-tissue regeneration. *Materials* **2019**, *14*, 568. [[CrossRef](#)]
10. Gotman, I.; Ben-David, D.; Unger, R.E.; Böse, T.; Gutmanas, E.Y.; Kirkpatrick, C.J. Mesenchymal stem cell proliferation and differentiation on load-bearing trabecular Nitinol scaffolds. *Acta Biomater.* **2013**, *9*, 8440–8448. [[CrossRef](#)]
11. Liu, B.; Lin, P.; Shen, Y.; Dong, Y. Porous bioceramics reinforced by coating gelatin. *J. Mater. Sci. Mater. Med.* **2008**, *19*, 1203–1207. [[CrossRef](#)]
12. Hutmacher, D.W. Scaffolds in tissue engineering bone and cartilage. *Biomaterials* **2000**, *21*, 2529–2543. [[CrossRef](#)]
13. Wu, S.; Liu, X.; Yeung, K.W.K.; Yang, X. Biomimetic porous scaffolds for bone tissue engineering. *Mater. Sci. Eng. R Rep.* **2014**, *80*, 1–36. [[CrossRef](#)]
14. Warnke, P.H. Rapid prototyping: Porous titanium alloy scaffolds produced by selective laser melting for bone tissue engineering. *Tissue Eng. Part C Methods* **2009**, *15*, 115–124. [[CrossRef](#)] [[PubMed](#)]
15. Van Bael, S. The effect of pore geometry on the in vitro biological behavior of human periosteum-derived cells seeded on selective laser-melted Ti6Al4V bone scaffolds. *Acta Biomater.* **2012**, *8*, 2824–2834. [[CrossRef](#)] [[PubMed](#)]
16. Sun, W.; Hu, X. Reasoning Boolean operation-based modeling for heterogeneous objects. *CAD Comput. Aided Des.* **2002**, *34*, 481–488. [[CrossRef](#)]
17. Choy, S.Y.; Sun, C.N.; Leong, K.F.; Wei, J. Compressive properties of functionally graded lattice structures manufactured by selective laser melting. *Mater. Des.* **2017**, *131*, 112–120. [[CrossRef](#)]
18. O'Brien, F.J.; Harley, B.A.; Waller, M.A.; Yannas, I.V.; Gibson, L.J.; Prendergast, P.J. The effect of pore size on permeability and cell attachment in collagen scaffolds for tissue engineering. *Technol. Health Care* **2007**, *15*, 3–17. [[CrossRef](#)]
19. Melchels, F.P.W.; Barradas, A.M.C.; Van Blitterswijk, C.A.; De Boer, J.; Feijen, J.; Grijpma, D.W. Effects of the architecture of tissue engineering scaffolds on cell seeding and culturing. *Acta Biomater.* **2010**, *6*, 4208–4217. [[CrossRef](#)]
20. Jessica, M.K.; Scott, J.H. Differential effects of designed scaffold permeability on chondrogenesis by chondrocytes and bone marrow stromal cells. *Biomaterials* **2010**, *31*, 279–287.
21. Furumoto, T.; Koizumi, A.; Alkahari, M.R.; Anayama, R.; Hosokawa, A.; Tanaka, R.; Ueda, T. Permeability and strength of a porous metal structure fabricated by additive manufacturing. *J. Mater. Process. Technol.* **2015**, *219*, 10–16. [[CrossRef](#)]
22. Syahrom, A.; Abdul Kadir, M.R.; Abdullah, J.; Öchsner, A. Permeability study of cancellous bone and its idealised structures. *Med. Eng. Phys.* **2015**, *37*, 77–86. [[CrossRef](#)] [[PubMed](#)]
23. Ochoa, I.; Sanz-Herrera, A.; Sanz-Herrera, J.M.; Doblaré, M.; Yunos, D.M.; Boccaccini, A.R. Permeability evaluation of 45S5 Bioglass®-based scaffolds for bone tissue engineering. *J. Biomech.* **2009**, *42*, 257–260. [[CrossRef](#)]
24. Sandino, C.; Krolczek, P.; McErlain, D.D.; Boyd, S.K. Predicting the permeability of trabecular bone by micro-computed tomography and finite element modeling. *J. Biomech.* **2014**, *47*, 3129–3134. [[CrossRef](#)] [[PubMed](#)]
25. Malachanne, E.; Dureisseix, D.; Cañadas, P.; Jourdan, F. Experimental and numerical identification of cortical bone permeability. *J. Biomech.* **2008**, *41*, 721–725. [[CrossRef](#)]
26. Chor, M.V.; Li, W. A permeability measurement system for tissue engineering scaffolds. *Meas. Sci. Technol.* **2007**, *18*, 208–216. [[CrossRef](#)]
27. Grimm, M.J.; Williams, J.L. Measurements of permeability in human calcaneal trabecular bone. *J. Biomech.* **1997**, *30*, 743–745. [[CrossRef](#)]
28. Beno, T.; Yoon, Y.J.; Cowin, S.C.; Fritton, S.P. Estimation of bone permeability using accurate microstructural measurements. *J. Biomech.* **2006**, *39*, 2378–2387. [[CrossRef](#)]
29. Kohles, S.S.; Roberts, J.B.; Upton, M.L.; Wilson, C.G.; Bonassar, L.J.; Schlichting, A.L. Direct perfusion measurements of cancellous bone anisotropic permeability. *J. Biomech.* **2001**, *34*, 1197–1202. [[CrossRef](#)]
30. Swider, P.; Conroy, M.; Pedrono, A.; Ambard, D.; Mantell, S.; Soballe, K. Use of high-resolution MRI for investigation of fluid flow and global permeability in a material with interconnected porosity. *J. Biomech.* **2007**, *40*, 2112–2118. [[CrossRef](#)]
31. Barba, D.; Alabort, E.; Reed, R.C. Synthetic bone: Design by additive manufacturing. *Acta Biomater.* **2019**, *97*, 637–656. [[CrossRef](#)] [[PubMed](#)]
32. Melchels, F.P.W.; Bertoldi, K.; Gabbrielli, R.; Velders, A.H.; Feijen, J.; Grijpma, D.W. Mathematically defined tissue engineering scaffold architectures prepared by stereolithography. *Biomaterials* **2010**, *31*, 6909–6916. [[CrossRef](#)]
33. Brennan, S.A.; Brabazon, D.; O'Byrne, J.M. Effect of vibration on the shear strength of impacted bone graft in revision hip surgery. *J. Bone Jt. Surg. Ser. B* **2011**, *93-B*, 755–759. [[CrossRef](#)]
34. Mcmenamain, P.G.; Quayle, M.R.; Mchenry, C.R.; Adams, J.W. The production of anatomical teaching resources using three-dimensional (3D) printing technology. *Anat. Sci. Educ.* **2014**, *7*, 479–486. [[CrossRef](#)] [[PubMed](#)]

35. Msallem, B.; Sharma, N.; Cao, S.; Halbeisen, F.S.; Zeilhofer, H.F.; Thieringer, F.M. Evaluation of the Dimensional Accuracy of 3D-Printed Anatomical Mandibular Models Using FFF, SLA, SLS, MJ, and BJ Printing Technology. *J. Clin. Med.* **2020**, *9*, 817. [CrossRef] [PubMed]
36. Kim, C.G.; Han, K.S.; Lee, S.; Kim, M.C.; Kim, S.Y.; Nah, J. Fabrication of Biocompatible Polycaprolactone–Hydroxyapatite Composite Filaments for the FDM 3D Printing of Bone Scaffolds. *Appl. Sci.* **2021**, *11*, 6351.
37. Surface Energy Methods Summary. Available online: <https://www.jasoint.co.jp/products/contact-angle/pdf/ap72.pdf> (accessed on 1 May 2021).
38. Kruczek, B. Carman–Kozeny Equation. In *Encyclopedia of Membranes*; Drioli, E., Giorno, L., Eds.; Springer: Berlin/Heidelberg, Germany, 2014.
39. Heintl, P.; Müller, L.; Körner, C.; Singer, R.F. Cellular Ti-6Al-4V structures with interconnected macro porosity for bone implants fabricated by selective electron beam melting. *Acta Biomater.* **2008**, *4*, 1536–1544. [CrossRef] [PubMed]
40. Zein, I.; Hutmacher, D.W.; Tan, K.C.; Teoh, S.H. Fused deposition modeling of novel scaffold architectures for tissue engineering applications. *Biomaterials* **2002**, *23*, 1169–1185. [CrossRef]
41. Seitz, H.; Rieder, W.; Irsen, S.; Leukers, B.; Tille, C. Three-dimensional printing of porous ceramic scaffolds for bone tissue engineering. *J. Biomed. Mater. Res. Part B Appl. Biomater.* **2005**, *74*, 782–788. [CrossRef]
42. Liu, Y.; Lu, Y.; Tian, X.; Cui, G.; Zhao, Y.; Yang, Q.; Yu, S.; Xing, G.; Zhang, B. Segmental bone regeneration using an rhBMP-2-loaded gelatin/nanohydroxyapatite/fibrin scaffold in a rabbit model. *Biomaterials* **2009**, *30*, 6276–6285. [CrossRef]
43. Rosenson, R.S.; McCormick, A.; Uretz, E.F. Distribution of blood viscosity values and biochemical correlates in healthy adults. *Clin. Chem.* **1996**, *72*, 1189–1195. [CrossRef]
44. ASTM D695-15; Standard Test Method for Compressive Properties of Rigid Plastics. *ASTM International 8 January 2008*. Available online: <https://www.astm.org/Standards/D695.htm> (accessed on 1 May 2021).
45. Nauman, E.A.; Fong, K.E.; Keaveny, T.M. Dependence of Intertrabecular Permeability on Flow Direction and Anatomic Site. *Ann. Biomed. Eng.* **1999**, *27*, 517–524. [CrossRef] [PubMed]
46. Beaudoin, A.J.; Mihalko, W.M.; Krause, W.R. Finite element modelling of polymethylmethacrylate flow through cancellous bone. *J. Biomech.* **1991**, *24*, 127–129. [PubMed]
47. Ochia, R.S.; Ching, R.P. Hydraulic resistance and permeability in human lumbar vertebral bodies. *J. Biomech. Eng.* **2002**, *124*, 533–537. [CrossRef]
48. Wu, Y.C.; Lee, T.M.; Chiu, K.H.; Shaw, S.Y.; Yang, C.Y. A comparative study of the physical and mechanical properties of three natural corals based on the criteria for bone-tissue engineering scaffolds. *J. Mater. Sci. Mater. Med.* **2009**, *20*, 1273–1280. [CrossRef]
49. Lipowiecki, M.; Ryvolova, M.; Tottosi, A.; Kolmer, N.; Naher, S.; Brennan, S.; Vazquez, M.; Brabazon, D. Permeability of rapid prototyped artificial bone scaffold structures. *J. Biomed. Mater. Res. Part A* **2014**, *102*, 4127–4135.
50. Li, Y.; Yang, C.; Zhao, H.; Qu, S.; Li, Y. New developments of ti-based alloys for biomedical applications. *Materials* **2014**, *7*, 1709–1800. [CrossRef]
51. Zaharin, H.A.; Rani, A.M.A.; Azam, I.F.; Ginta, T.L.; Salliha, N.; Ahmad, A.; Yunus, N.A.; Zulkifi, T.Z.A. Effect of Unit Cell Type and Pore Size on Porosity and Mechanical Behavior of Additively Manufactured Ti6Al4V Scaffolds. *Materials* **2018**, *11*, 2402. [CrossRef] [PubMed]